PERGAMON

International Journal of Solids and Structures 38 (2001) 1459–1481

INTERNATIONAL JOURNAL OF SOLIDS and STRUCTURES

www.elsevier.com/locate/ijsolstr

A new analytic solution for the diametral point load strength test on finite solid circular cylinders

K.T. Chau *, X.X. Wei

Department of Civil and Structural Engineering, The Hong Kong Polytechnic University, Hung Hom, Kowloon, Hong Kong, China

Received 23 April 1999; in revised form 17 March 2000

Abstract

This paper presents an exact analytic solution for a finite isotropic circular cylinder of diameter D and length $2L$ subjected to the diametral point load strength test (PLST). Two displacement functions are introduced to uncouple the equations of equilibrium, and two new series expressions for these functions are proposed in terms of the Bessel and modified Bessel functions of the first kind, the trigonometric functions and the hyperbolic functions. The contact stresses between the curved surface of the cylinder and the spherical heads of the indentors are expanded into double Fourier series expansion in order to match the limiting values of the stress field on the boundary. Our numerical results show that tensile stress concentrations are developed near the point loads, compared to the roughly uniform tensile stress at the central portion of the line between the two point loads. The pattern of tensile stress distribution along this line resembles that obtained for a sphere under the diametral PLST (Chau, K.T., Wei, X.X., 1999. Int. J. Solids and Struct. 36 (29), 4473–4496) and a cylinder under the axial PLST (Wei, X.X., et al., 1999. J. Eng. Mech. ASCE 125 (12), 1349–1357). The maximum tensile stress decreases with the increase of Poisson's ratio, the contact area, the radius of the spherical heads of the indentors, but increases with the diameter of the cylinder. It also decreases drastically with the increase of L/D for short cylinders (say $L/D < 0.4$), but remains roughly constant when L/D is long enough (say $L/D > 0.7$). Both the predicted size and shape effects of specimens on the diametral PLST agree with our experimental observations.

Keywords: Diametral point load strength test; Finite solid cylinders; Non-axisymmetric deformation; Stress analysis; Displacement functions

1. Introduction

Indirect tensile strength is more useful than direct tensile strength in rock mechanics application, partly because tensile stress field in rock mass is usually induced indirectly by compressive deviatoric stresses and partly because direct tension is difficult to apply to rock specimens without inducing any eccentric moments. The point load strength test (PLST) is one of the most popular indirect tensile strength tests used in

* Corresponding author. Tel.: +852-2766-6015; fax: +852-2334-6389.
E-mail address: cektchau@polyu.edu.hk (K.T. Chau).

0020-7683/01/$ - see front matter
PII: S0020-7683(00)00122-0

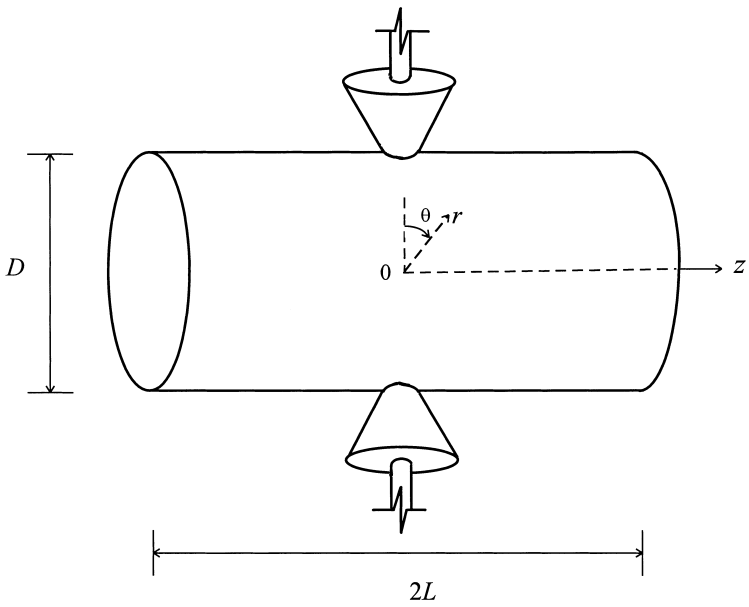

Fig. 1. A cylindrical rock specimen subjected to the diametral PLST. The origin is at the center of the cylinder and the indentors act along a diameter passing through the origin.

rock engineering. The strength index measured in this test is called the point load strength index (PLSI), which is a measure of the indirect tensile strength and has been correlated empirically to both the tensile strength and compressive strength of rock. The PLST has been applied most commonly to cylindrical specimens, either axially or diametrally. But as remarked by Chau (1998), the diametral PLST is usually preferred (Bieniawski, 1975; Hassani et al., 1980), and thus the focus of the present paper is on the stress analysis for cylinders under the diametral PLST given in Fig. 1.

The diametral PLST has been investigated by many experimental studies (see the review by Chau (1998)), but there are relatively few theoretical works on the PLST. Theoretical analyses have been carried out for the PLST on isotropic spheres (Sternberg and Rosenthal, 1952; Hiramatsu and Oka, 1966) and anisotropic spheres (Wei and Chau, 1998; Chau and Wei, 1999), for the axial PLST on solid cylinders (Peng, 1976; Wijk, 1978; Chau and Wong, 1996; Wei et al., 1999), and for the diametral PLST on solid cylinders (Wijk, 1980; Chau, 1998).

In particular, regarding the tensile stress concentration in cylinders under the diametral PLST, Wijk (1980) provided an approximation for the tensile stress at the center of a solid circular cylinder. The tensile stress distribution along the line joining the two applied point loads is interpolated between the tensile stresses obtained from the solution for the PLST on spheres by Hiramatsu and Oka (1996) and from the solution for the axial PLST on finite circular plates by Wijk (1978) (see Fig. 2 of Wijk (1980)). Recently, Chau (1998) obtained an analytic solution for a finite cylinder under the diametral PLST with shear displacements constrained on the two end surfaces, whereas in actual PLST the end boundaries are shear traction-free. The main reason why Chau (1998) considered this kind of modified end boundary is to simplify the problem and to make it mathematically tractable. To date, there is no exact analysis available for evaluating the stresses within a finite solid cylinder under the diametral PLST.

In addition, the stress analysis for elastic isotropic cylinders under various boundary conditions is one of the most fundamental problems in theoretical elasticity and has a rich history in the field of solid me-

chanics. As remarked by Filon (1902), the general stress analysis (including non-axisymmetric) for an infinite circular cylinder subjected to an arbitrary surface load was considered independently by Pochhammer (1876) and Chree (1889). One of the commonly investigated problems for finite cylinders under axisymmetric deformation is the compression of cylinders between two blocks at the end surface. This problem was first considered by Filon (1902), and subsequently by many others (see the review by Chau (1997)). More general stress analyses for axisymmetric problems for circular cylinders were considered by Saito (1952, 1954) and Ogaki and Nakajima (1983). The only analysis for non-axisymmetric deformation of finite cylinders is the approximate solution by Dougall (1914), who introduced three displacement functions. There is, however, no exact analysis for solving non-axisymmetric problems for finite cylinders involving loads on the curved surface and with traction-free end surfaces. The stress analysis for cylinders under the diametral PLST (present problem) is one of these unsolved non-axisymmetric problems for finite circular cylinders. As mentioned earlier, the only approximation for a finite cylinder under the diametral PLST is the solution by Wijk (1980) and Chau (1998).

Therefore, the objective of this paper is to present a new analytic solution for finite cylinders under the diametral PLST. Although the problem considered here is physically similar to that considered by Chau (1998), the solution forms for the displacement functions to be introduced here are completely different. In fact, the proper choice of these solution forms is the most challenging problem in the analysis of the present cylinder problem. The solution form to be given here is original as no appropriate solution form has been proposed previously for non-axisymmetric problems of solid cylinders, including the problem of the diametral PLST. In addition, the point loads are modeled more realistically by indentors acting upon the solid cylinders in this study (Fig. 1). The contact stress between the curved surface of the cylinder and the spherical heads of the indentors is expanded into a double Fourier series so as to match the boundary values of the internal stress field.

The results of the study should provide the fundamental understanding of the tensile stress field within a finite cylinder under the diametral PLST. In addition to the practical application to the diametral PLST, the present study also provides a general solution technique for the stress analysis for cylinders subjected to arbitrary normal stress on the curved surface and zero traction on the two end surfaces. This solution technique is particularly useful when we consider problems involving short cylinders and with significant end effect.

2. Mathematical formulation of the problem

The finite cylindrical specimen considered is of radius R (or diameter D) and length $2L$, and is assumed to be homogeneous, linear elastic and isotropic. The origin and z-axis of the cylindrical polar coordinate (r, θ, z) system coincide with the center and the axis of symmetry of the specimen as shown in Fig. 1. The basic equations for elastic solids, including the Hooke's law and equilibrium equations, have been given in Chau (1998) and will not be repeated here.

When the specimen is subjected to the diametral PLST, all the surfaces of the specimen are traction-free except for the contact stress within the elliptical contact zones between the spherical heads of the indentors and the curved surface of the cylinder (Fig. 1). More specifically, the boundary conditions for the finite cylinder under the diametral PLST are (Chau, 1998)

$$\sigma_{zz} = 0, \qquad \sigma_{zr} = 0, \qquad \sigma_{z\theta} = 0 \tag{1}$$

on $z = \pm L$; and

$$\sigma_{rz} = 0, \qquad \sigma_{r\theta} = 0, \tag{2}$$

$$\sigma_{rr}(R,\theta,z)=\begin{cases}-\frac{3P}{2\pi ab}(1-\frac{R^2\theta^2}{a^2}-\frac{z^2}{b^2})^{1/2} & \text{for } |z|\leqslant b, \text{ and } |\theta|\leqslant \frac{a}{R}\left(1-\frac{z^2}{b^2}\right)^{1/2} \text{ or } |\pi-\theta|\leqslant \frac{a}{R}\left(1-\frac{z^2}{b^2}\right)^{1/2},\\ 0 & \text{for } |z|>b, \text{ and } |\theta|>\frac{a}{R}\left(1-\frac{z^2}{b^2}\right)^{1/2} \text{ or } |\pi-\theta|>\frac{a}{R}\left(1-\frac{z^2}{b^2}\right)^{1/2}\end{cases} \tag{3}$$

on $r=R$, where P is the magnitude of the applied point load. The contact zone parameters (i.e. a and b) can be evaluated by Eq. (13) of Chau (1998). In obtaining Eq. (2), we have assumed the contact to be smooth and frictionless. A double Fourier expansion with respect to z and θ is applied to the contact stresses (Chau, 1998)

$$\sigma_{rr}(R,z,\theta)=\sum_{n=0}^{\infty}\sum_{m=0}^{\infty}\chi D_{mn}\cos(\eta_m z)\cos(2n\theta), \tag{4}$$

where

$$\chi=\begin{cases}1/4 & \text{for } m=n=0,\\ 1/2 & \text{for } m=0, n\neq 0 \text{ or } m\neq 0, n=0,\\ 1 & \text{for } n>0 \text{ and } m>0,\end{cases} \tag{5}$$

$$D_{mn}=-\frac{3P}{\pi RL}\left[\int_0^{\pi/2}\sin^3\beta\cos(\eta_m b\cos\beta)J_0(\zeta\sin\beta)\,\mathrm{d}\beta+\int_0^{\pi/2}\sin^3\beta\cos(\eta_m b\cos\beta)J_2(\zeta\sin\beta)\,\mathrm{d}\beta\right], \tag{6}$$

where

$$\zeta=2na/R \quad \text{and} \quad \eta_m=\frac{m\pi}{L}. \tag{7}$$

Note that these expressions are similar to those given by Chau (1998) after some minor mistakes are corrected.

3. Series solution for the displacement functions

The following two displacement functions Φ and Ψ are adopted from Chau (1998) (except for a minor typing error):

$$u_r=\frac{\partial^2\Phi}{\partial r\partial z}+\frac{1}{r}\frac{\partial\Psi}{\partial\theta}, \quad u_\theta=\frac{1}{r}\frac{\partial^2\Phi}{\partial\theta\partial z}-\frac{\partial\Psi}{\partial r}, \quad u_z=-\left[2(1-\nu)\nabla_1\Phi+(1-2\nu)\frac{\partial^2\Phi}{\partial z^2}\right], \tag{8}$$

where

$$\nabla_1=\frac{1}{r}\frac{\partial}{\partial r}\left(r\frac{\partial}{\partial r}\right)+\frac{1}{r^2}\frac{\partial^2}{\partial\theta^2}. \tag{9}$$

By employing Eq. (8), it can be shown that the three equilibrium equations are converted to the following two uncoupled partial differential equations for Φ and Ψ

$$\nabla^4\Phi=\nabla^2\nabla^2\Phi=0, \quad \nabla^2\Psi=0, \tag{10}$$

where ∇^2 is the Laplacian operator, or $\nabla^2=\nabla_1+\partial^2/\partial z^2$. By applying the two displacement functions given in Eq. (8), the stress components can be expressed in terms of the two displacement functions Φ and Ψ, which have been given in Eqs. (20)–(24) of Chau (1998). However, minor typing mistakes were found in Chau (1998); thus, Appendix A reports the corrected expressions for the sake of completeness.

The most important step of the analysis is to assume appropriate forms for the two displacement functions such that both the governing equations (10) and the boundary conditions (1)–(3) can be satisfied. After tedious steps of trial and error, the following two series expressions for Φ and Ψ are proposed:

$$\Phi = -\frac{1}{2G}\left\{A_0\frac{z^3}{6} + C_0\frac{z}{2}r^2 + \sum_{n=0}^{\infty}\left\{H_{0n}r^{2n}z + \sum_{m=1}^{\infty}\frac{1}{\eta_m^3}\left[A_{mn}r\frac{\partial I_{2n}(\eta_m r)}{\partial r} + B_{mn}I_{2n}(\eta_m r)\right]\sin(\eta_m z)\right.\right.$$
$$\left.\left. + \sum_{s=1}^{\infty}\frac{1}{\gamma_s^3}[C_{sn}\sinh(\gamma_s z) + D_{sn}\gamma_s z\cosh(\gamma_s z)]J_{2n}(\gamma_s r)\right\}\cos(2n\theta)\right\}, \tag{11}$$

$$\Psi = -\frac{1}{2G}\left\{\sum_{n=0}^{\infty}\left[E_{0n}r^{2n} + \sum_{m=1}^{\infty}\frac{E_{mn}}{\eta_m^2}I_{2n}(\eta_m r)\cos(\eta_m z)\right]\sin(2n\theta)\right\}, \tag{12}$$

where $\eta_m = m\pi/L$, $\gamma_s = \lambda_s/R$, and λ_s is the sth root of $J'_{2n}(\lambda_s) = 0$ (i.e. derivative of the Bessel function), $J_{2n}(x)$ and $I_{2n}(x)$ are the Bessel and modified Bessel functions of the first kind of order $2n$ respectively, and $A_0, C_0, H_{0n}, E_{0n}, A_{mn}, B_{mn}, C_{sn}, D_{sn}$ and E_{mn} are unknown coefficients to be determined by the boundary conditions (1)–(3). When we chose the present form of Eqs. (11) and (12), we tried to include all meaningful terms (i.e. those leading to non-zero and relevant stress field) that are solutions to the governing equations (10). Since the periodicity of the pair of point loads on the circumference is π (Fig. 1), the periodicity of displacement functions Φ and Ψ in θ must also be π (i.e. $\sin(2n\theta)$ and $\cos(2n\theta)$). The first two terms in Eq. (11) lead to constant normal stresses (it is evident from the expressions of stresses to be given later), and the first term within the summation for index n results from considering the term $m = 0$ in the next summation. The first term in the summation for index n in Eq. (12) results from considering the term $m = 0$ in the next summation. It is straightforward to show that the forms of Φ and Ψ given in Eqs. (11) and (12) satisfy the governing equations (10) identically. A major difference between Eq. (11) and the corresponding form given in Eq. (32) of Chau (1998) is the inclusion of the additional summation for index s involving hyperbolic functions $\sinh(\gamma_s z)$ and $\cosh(\gamma_s z)$.

In the analysis by Chau (1998), the solution of Eq. (10) is given in the form of the product of the modified Bessel function and sin/cosine. Actually, there is one more general solution for the first part of Eq. (10) which can be expressed as the product of the Bessel functions and the hyperbolic functions. Although this latter form has been proposed by Schiff (1883) (cited by Filon, 1902), and has subsequently been adopted by Saito (1952, 1954) and Ogaki and Nakajima (1983), it should be emphasized here that the present form for Φ given in Eq. (11) is more general than the corresponding functions given by Schiff (Saito (1952, 1954) or Ogaki and Nakajima (1983)) because the present form is for the *non-axisymmetric* case whilst those by the previous workers are restricted for axisymmetric cases. For example, in axisymmetric cases the modified Bessel functions involved are of zero and first orders and all θ-dependent terms do not exist, whereas in the present analysis the Bessel and modified Bessel functions are of order $2n$ and sin or cosine dependency exists. Furthermore, the second displacement function Ψ does not exist (or is identically zero) in the axisymmetric case. Thus, the form for Ψ is completely new.

If $C_{sn} = D_{sn} = C_0 = A_0 = H_{0n} = E_{0n} = 0$, the two displacement functions Φ and Ψ given in Eqs. (11) and (12) reduce to the corresponding expressions by Chau (1998).

4. General expressions for stresses

Substitution of Eqs. (11) and (12) into Eqs. (A.1)–(A.6) given in Appendix A yields the following expressions for the stress components

$$\sigma_{rr} = (2\nu-1)C_0 + \nu A_0 + \sum_{n=0}^{\infty}\Bigg\{ -2n(2n-1)(H_{0n}+E_{0n})r^{2n-2} + \sum_{m=1}^{\infty}\Bigg\{ A_{mn}\Bigg[2\nu I_{2n}(\eta_m r) - \frac{1}{\eta_m^2}\frac{\partial^2}{\partial r^2}\left(r\frac{\partial I_{2n}(\eta_m r)}{\partial r}\right)\Bigg] - \frac{B_{mn}}{\eta_m^2}\frac{\partial^2 I_{2n}(\eta_m r)}{\partial r^2} - \frac{2nE_{mn}}{\eta_m^2}\frac{\partial}{\partial r}\left(\frac{I_{2n}(\eta_m r)}{r}\right)\Bigg\}\cos(\eta_m z) + \sum_{s=1}^{\infty}\Bigg\{[(C_{sn}(2\nu+1)D_{sn})\cosh(\gamma_s z) + D_{sn}\gamma_s z\sinh(\gamma_s z)]J_{2n}(\gamma_s r) + [(C_{sn}+D_{sn})\cosh(\gamma_s z) + D_{sn}\gamma_s z\sinh(\gamma_s z)]\left[\frac{1}{\gamma_s^2 r}\frac{\partial J_{2n}(\gamma_s r)}{\partial r} - \frac{4n^2}{\gamma_s^2 r^2}J_{2n}(\gamma_s r)\right]\Bigg\}\Bigg\}\cos(2n\theta), \tag{13}$$

$$\sigma_{\theta\theta} = (2\nu-1)C_0 + \nu A_0 + \sum_{n=0}^{\infty}\Bigg\{ 2n(2n-1)(H_{0n}+E_{0n})r^{2n-2} + \sum_{m=1}^{\infty}\Bigg\{ A_{mn}\Bigg[2\nu I_{2n}(\eta_m r) - \frac{1}{\eta_m^2}\frac{1}{r}\frac{\partial}{\partial r}\left(r\frac{\partial I_{2n}(\eta_m r)}{\partial r}\right) + \frac{4n^2}{\eta_m^2 r}\frac{\partial I_{2n}(\eta_m r)}{\partial r}\Bigg] - \frac{B_{mn}}{\eta_m^2}\left[\frac{1}{r}\frac{\partial I_{2n}(\eta_m r)}{\partial r} - \frac{4n^2}{r^2}I_{2n}(\eta_m r)\right] + \frac{2nE_{mn}}{\eta_m^2}\frac{\partial}{\partial r}\left(\frac{I_{2n}(\eta_m r)}{r}\right)\Bigg\}\cos(\eta_m z) + \sum_{s=1}^{\infty}\Bigg\{2\nu D_{sn}\cosh(\gamma_s z)J_{2n}(\gamma_s r) - [(C_{sn}+D_{sn})\cosh(\gamma_s z) + D_{sn}\gamma_s z\sinh(\gamma_s z)]\left[\frac{1}{\gamma_s^2 r}\frac{\partial J_{2n}(\gamma_s r)}{\partial r} - \frac{4n^2}{\gamma_s^2 r^2}J_{2n}(\gamma_s r)\right]\Bigg\}\Bigg\}\cos(2n\theta), \tag{14}$$

$$\sigma_{zz} = 2(2-\nu)C_0 + (1-\nu)A_0 + \sum_{n=0}^{\infty}\Bigg\{\sum_{m=1}^{\infty}\Bigg\{ A_{mn}\left[2(2-\nu)I_{2n}(\eta_m r) + r\frac{\partial I_{2n}(\eta_m r)}{\partial r}\right] + B_{mn}I_{2n}(\eta_m r)\Bigg\}\cos(\eta_m z) - \sum_{s=1}^{\infty}[(C_{sn}+(2\nu-1)D_{sn})\cosh(\gamma_s z) + D_{sn}\gamma_s z\sinh(\gamma_s z)]J_{2n}(\gamma_s r)\Bigg\}\cos(2n\theta), \tag{15}$$

$$\sigma_{rz} = \sum_{n=0}^{\infty}\Bigg\{\sum_{m=1}^{\infty}\Bigg\{ -\frac{A_{mn}}{\eta_m}\left[2(\nu-1)\frac{\partial I_{2n}(\eta_m r)}{\partial r} - \frac{\partial}{\partial r}\left(r\frac{\partial I_{2n}(\eta_m r)}{\partial r}\right)\right] + \frac{B_{mn}}{\eta_m}\frac{\partial I_{2n}(\eta_m r)}{\partial r} + \frac{nE_{mn}}{\eta_m}\frac{I_{2n}(\eta_m r)}{r}\Bigg\}\sin(\eta_m z) - \sum_{s=1}^{\infty}\Bigg\{\frac{1}{\gamma_s}[(C_{sn}+2\nu D_{sn})\sinh(\gamma_s z) + D_{sn}\gamma_s z\cosh(\gamma_s z)]\frac{\partial J_{2n}(\gamma_s r)}{\partial r}\Bigg\}\Bigg\}\cos(2n\theta), \tag{16}$$

$$\sigma_{z\theta}=\sum_{n=0}^{\infty}\Bigg\{\sum_{m=1}^{\infty}\Bigg\{\frac{2nA_{mn}}{\eta_m}\left[2(\nu-1)\frac{I_{2n}(\eta_m r)}{r}-\frac{\partial I_{2n}(\eta_m r)}{\partial r}\right]-\frac{2nB_{mn}}{\eta_m}\frac{I_{2n}(\eta_m r)}{r}$$
$$-\frac{E_{mn}}{2\eta_m}\frac{\partial I_{2n}(\eta_m r)}{\partial r}\Bigg\}\sin(\eta_m z)+\sum_{s=1}^{\infty}\Bigg\{\frac{2n}{\gamma_s}[(C_{sn}+2\nu D_{sn})\sinh(\gamma_s z)$$
$$+D_{sn}\gamma_s z\cosh(\gamma_s z)]\frac{J_{2n}(\gamma_s r)}{r}\Bigg\}\Bigg\}\sin(2n\theta), \tag{17}$$

$$\sigma_{r\theta}=\sum_{n=0}^{\infty}\Bigg\{2n(2n-1)(H_{0n}-E_{0n})r^{2n-2}+\sum_{m=1}^{\infty}\Bigg\{\frac{2nA_{mn}}{\eta_m^2}\frac{\partial^2 I_{2n}(\eta_m r)}{\partial r^2}+\frac{2nB_{mn}}{\eta_m^2}\left[\frac{1}{r}\frac{\partial I_{2n}(\eta_m r)}{\partial r}\right.$$
$$\left.-\frac{1}{r^2}I_{2n}(\eta_m r)\right]+\frac{E_{mn}}{2\eta_m^2}\left[-\frac{1}{r}\frac{\partial I_{2n}(\eta_m r)}{\partial r}+\frac{4n^2}{r^2}I_{2n}(\eta_m r)+\frac{\partial^2 I_{2n}(\eta_m r)}{\partial r^2}\right]\Bigg\}\cos(\eta_m z)$$
$$+\sum_{s=1}^{\infty}\frac{2n}{\gamma_s^2}[(C_{sn}+D_{sn})\cosh(\gamma_s z)+D_{sn}\gamma_s z\sinh(\gamma_s z)]\left[\frac{1}{r}\frac{\partial J_{2n}(\gamma_s r)}{\partial r}-\frac{1}{r^2}J_{2n}(\gamma_s r)\right]\Bigg\}\sin(2n\theta). \tag{18}$$

5. Determination of unknown coefficients

Specializing the shear stresses (16) and (17) to the end boundary conditions given in Eq. (1) (i.e. σ_{rz} and $\sigma_{z\theta}=0$ on $z=\pm L$), we have

$$(C_{sn}+2\nu D_{sn})\sinh(\gamma_s L)+D_{sn}\gamma_s L\cosh(\gamma_s L)=0. \tag{19}$$

This equation can be rewritten as

$$\frac{C_{sn}}{2\nu\sinh(\gamma_s L)+\gamma_s L\cosh(\gamma_s L)}=\frac{D_{sn}}{-\sinh(\gamma_s L)}=-\frac{G_{sn}}{\Lambda_s}, \tag{20}$$

where G_{sn} and Λ_s are constants introduced to simplify the equations involved in the subsequent analysis. Note that because there is only one unknown constant for the first term of Eq. (20), Λ_s is only an arbitrary constant to scale G_{sn} (which is to be fixed later). Then, the constants C_{sn} and D_{sn} can be re-written in terms of the newly introduced constants as

$$C_{sn}=-\frac{G_{sn}}{\Lambda_s}[2\nu\sinh(\gamma_s L)+\gamma_s L\cosh(\gamma_s L)], \tag{21}$$

$$D_{sn}=\frac{G_{sn}}{\Lambda_s}\sinh(\gamma_s L). \tag{22}$$

Substituting Eqs. (21) and (22) into Eq. (15), then specializing the resulting stress to $z=\pm L$, we have

$$\sigma_{zz}=2(2-\nu)C_0+(1-\nu)A_0+\sum_{n=0}^{\infty}\Bigg\{\sum_{m=1}^{\infty}\{A_{mn}[2(2-\nu-n)I_{2n}(\eta_m r)+\eta_m r I_{2n-1}(\eta_m r)]$$
$$+B_{mn}I_{2n}(\eta_m r)\}(-1)^m+\sum_{s=1}^{\infty}\frac{G_{sn}}{\Lambda_s}[\gamma_s L+\sinh(\gamma_s L)\cosh(\gamma_s L)]J_{2n}(\gamma_s r)\Bigg\}\cos(2n\theta) \tag{23}$$

The first of the boundary conditions (1) requires that the normal stress is identically zero on the two end surfaces (i.e. $\sigma_{zz}=0$ on $z=\pm L$), independent of both r and θ. In view of this, we expand all terms with r-dependency (i.e. the modified Bessel functions) in Eq. (23) into series expansion of Bessel function (Watson, 1944) and then assume the following value for Λ_s:

$$\Lambda_s = \gamma_s L + \sinh(\gamma_s L)\cosh(\gamma_s L). \tag{24}$$

We should emphasize that Λ_s is simply an additional constant introduced in Eq. (20) such that the final expression can be represented in a more compact form. Therefore, it can be set arbitrarily. Subsequently, Eq. (23) is simplified to the following compact form:

$$\sigma_{zz} = 2(2-v)C_0 + (1-v)A_0 + \sum_{n=0}^{\infty}\sum_{s=1}^{\infty}\left\{ G_{sn} + \sum_{m=1}^{\infty}\{A_{mn}[2(2-v-n)T_{ms} + U_{ms}] + B_{mn}T_{ms}\} \times (-1)^m \right\} J_{2n}(\gamma_s r)\cos(2n\theta), \tag{25}$$

where

$$T_{ms} = \frac{2\lambda_s^2}{(\lambda_s^2 - 4n^2)[(\eta_m R)^2 + \lambda_s^2]J_{2n}^2(\lambda_s)}[\eta_m R I_{2n+1}(\eta_m R)J_{2n}(\lambda_s) + \lambda_s I_{2n}(\eta_m R)J_{2n+1}(\lambda_s)], \tag{26}$$

$$U_{ms} = \frac{2\lambda_s^2\eta_m R}{(\lambda_s^2 - 4n^2)[(\eta_m R)^2 + \lambda_s^2]J_{2n}^2(\lambda_s)}\left\{ \frac{(4n-2)\eta_m R}{(\eta_m R)^2 + \lambda_s^2}[\eta_m R I_{2n+1}(\eta_m R)J_{2n}(\lambda_s) + \lambda_s I_{2n}(\eta_m R)J_{2n+1}(\lambda_s)] + \frac{4n\lambda_s}{(\eta_m R)^2 + \lambda_s^2}[\eta_m R I_{2n}(\eta_m R)J_{2n-1}(\lambda_s) + \lambda_s I_{2n-1}(\eta_m R)J_{2n}(\lambda_s)] + \eta_m R I_{2n}(\eta_m R)J_{2n}(\lambda_s) - \lambda_s I_{2n-1}(\eta_m R)J_{2n-1}(\lambda_s) \right\}. \tag{27}$$

The procedure in obtaining Eqs. (26) and (27) is reported briefly in Appendix B for the sake of completeness. Finally, the end boundary condition ($\sigma_{zz}=0$ on $z=\pm L$) yields the following equations for the unknown coefficients:

$$2(2-v)C_0 + (1-v)A_0 = 0, \tag{28}$$

$$G_{sn} + \sum_{m=1}^{\infty}\{A_{mn}[2(2-v-n)T_{ms} + U_{ms}] + B_{mn}T_{ms}\}(-1)^m = 0. \tag{29}$$

So far, all boundary conditions on the two end surfaces given in Eq. (1) have been considered. The next step is to ensure that the boundary conditions (2) and (3) on the curved surface will be satisfied. Substitution of Eq. (16) into the shear traction-free condition (2) (i.e., $\sigma_{rz}=0$ on $r=R$) leads to

$$-\frac{A_{mn}}{\eta_m}\left[(2v-3)\left(\frac{\partial I_{2n}(\eta_m R)}{\partial r} - R\frac{\partial^2 I_{2n}(\eta_m R)}{\partial r^2}\right) + \frac{B_{mn}}{\eta_m}\frac{\partial I_{2n}(\eta_m R)}{\partial r} + \frac{nE_{mn}}{\eta_m}\frac{I_{2n}(\eta_m R)}{R}\right] = 0. \tag{30}$$

To consider the boundary condition for the shear stress $\sigma_{r\theta}$, we, by applying a similar technique leading to the results given in Eqs. (28) and (29), substitute Eqs. (21) and (22) into Eq. (18) and specialize the result on $r = R$. Then, all $\cosh(\gamma_s z)$ and $\gamma_s z \sinh(\gamma_s z)$ terms involved are expanded into series of $\cos(\eta_m z)$ and the final form is

$$\begin{aligned}\sigma_{r\theta} = \sum_{n=0}^{\infty}\Bigg\{ & 2n(2n-1)(H_{0n}-E_{0n})R^{2n-2} + \sum_{S=1}^{\infty}\frac{4n\nu G_{sn}\sinh^2(\gamma_s L)}{\Lambda_s\gamma_s L}\frac{J_{2n}(\gamma_s R)}{\gamma_s^2 R^2} + \sum_{m=1}^{\infty}\Bigg\{\frac{2nA_{mn}}{\eta_m^2}\frac{\partial^2 I_{2n}(\eta_m R)}{\partial r^2} \\ & + \frac{2nB_{mn}}{\eta_m^2}\left[\frac{1}{R}\frac{\partial I_{2n}(\eta_m R)}{\partial r} - \frac{1}{R^2}I_{2n}(\eta_m R)\right] + \frac{E_{mn}}{2\eta_m^2}\left[-\frac{1}{R}\frac{\partial I_{2n}(\eta_m R)}{\partial r} + \frac{4n^2}{R^2}I_{2n}(\eta_m R) + \frac{\partial^2 I_{2n}(\eta_m R)}{\partial r^2}\right] \\ & - \sum_{s=1}^{\infty}\frac{G_{sn}}{\Lambda_s}\frac{8n(-1)^m\sinh^2(\gamma_s L)}{\gamma_s L(\gamma_s^2+\eta_m^2)}\frac{J_{2n}(\gamma_s R)}{R^2}\left[\frac{\eta_m^2}{\gamma_s^2+\eta_m^2} - \nu\right]\Bigg\}\cos(\eta_m z)\Bigg\}\sin(2n\theta). \end{aligned} \tag{31}$$

Subsequently, we can apply the second of the boundary conditions (2) to Eq. (31). That is, the shear stress $\sigma_{r\theta}$ on the curved boundary is identically zero for any value of z and θ, and this leads to

$$2n(2n-1)(H_{0n}-E_{0n})R^{2n-2} = -\sum_{S=1}^{\infty}\frac{4n\nu G_{sn}\sinh^2(\gamma_s L)}{\Lambda_s\gamma_s L}\frac{J_{2n}(\gamma_s R)}{\gamma_s^2 R^2}, \tag{32}$$

$$\begin{aligned}& \frac{2nA_{mn}}{\eta_m^2}\frac{\partial^2 I_{2n}(\eta_m R)}{\partial r^2} + \frac{2nB_{mn}}{\eta_m^2}\left[\frac{1}{R}\frac{\partial I_{2n}(\eta_m R)}{\partial r} - \frac{1}{R^2}I_{2n}(\eta_m R)\right] + \frac{E_{mn}}{2\eta_m^2}\left[-\frac{1}{R}\frac{\partial I_{2n}(\eta_m R)}{\partial r} + \frac{4n^2}{R^2}I_{2n}(\eta_m R)\right. \\ & \left. + \frac{\partial^2 I_{2n}(\eta_m R)}{\partial r^2}\right] - \sum_{s=1}^{\infty}\frac{G_{sn}}{\Lambda_s}\frac{8n(-1)^m\sinh^2(\gamma_s L)}{\gamma_s L(\gamma_s^2+\eta_m^2)}\frac{J_{2n}(\gamma_s R)}{R^2}\left[\frac{\eta_m^2}{\gamma_s^2+\eta_m^2} - \nu\right] = 0. \end{aligned} \tag{33}$$

Note that Eq. (32) results from setting the first two terms of Eq. (31) to zero, and Eq. (33) results from setting the remaining terms to zero (since shear stress must be identically zero independent of the index m).

In order to satisfy the last boundary condition (3), we set $r = R$ in Eq. (13) to yield

$$\begin{aligned}\sigma_{rr} = (2\nu-1)C_0 + \nu A_0 + \sum_{n=0}^{\infty}\Bigg\{ & -2n(2n-1)(H_{0n}+E_{0n})R^{2n-2} + \sum_{m=1}^{\infty}\Bigg\{A_{mn}\Bigg[2\nu I_{2n}(\eta_m R) \\ & - \frac{1}{\eta_m^2}\left[2\frac{\partial^2 I_{2n}(\eta_m R)}{\partial r^2} + R\frac{\partial^3 I_{2n}(\eta_m R)}{\partial r^3}\right]\Bigg] - \frac{B_{mn}}{\eta_m^2}\frac{\partial^2 I_{2n}(\eta_m R)}{\partial r^2} + \frac{2nE_{mn}}{\eta_m^2}\left[\frac{I_{2n}(\eta_m R)}{R^2}\right. \\ & \left. - \frac{1}{R}\frac{\partial I_{2n}(\eta_m R)}{\partial r}\right]\Bigg\}\cos(\eta_m z) - \sum_{s=1}^{\infty}\Bigg\{[(C_{sn}+D_{sn})\cosh(\gamma_s z) + D_{sn}\gamma_s z\sinh(\gamma_s z)]\frac{4n^2}{\gamma_s^2 R^2}J_{2n}(\gamma_s R) \\ & + [(C_{sn}+(2\nu+1)D_{sn})\cosh(\gamma_s z) + D_{sn}\gamma_s z\sinh(\gamma_s z)]J_{2n}(\gamma_s R)\Bigg\}\Bigg\}\cos(2n\theta). \end{aligned} \tag{34}$$

Before we apply the boundary condition, we again substitute Eqs. (21) and (22) into Eq. (34) and expand all functions of z-dependency in terms of $\cos(\eta_m z)$,

$$\sigma_{rr} = (2\nu-1)C_0 + \nu A_0 + \sum_{n=0}^{\infty}\Bigg\{ -2n(2n-1)(H_{0n}+E_{0n})R^{2n-2} + \sum_{s=1}^{\infty}\frac{G_{sn}}{\Lambda_s}\frac{8n^2\gamma_s\sinh^2(\gamma_s L)}{\gamma_s L}\frac{J_{2n}(\gamma_s R)}{\gamma_s^2 R^2}$$
$$+\sum_{m=1}^{\infty}\Bigg\{A_{mn}\left[2\nu I_{2n}(\eta_m R) - \frac{1}{\eta_m^2}\left[2\frac{\partial^2 I_{2n}(\eta_m R)}{\partial r^2} + R\frac{\partial^3 I_{2n}(\eta_m R)}{\partial r^3}\right]\right] - \frac{B_{mn}}{\eta_m^2}\frac{\partial^2 I_{2n}(\eta_m R)}{\partial r^2}$$
$$+\frac{2nE_{mn}}{\eta_m^2}\left[\frac{I_{2n}(\eta_m R)}{R^2} - \frac{1}{R}\frac{\partial I_{2n}(\eta_m R)}{\partial r}\right] - \sum_{s=1}^{\infty}\frac{G_{sn}}{\Lambda_s}\frac{4\gamma_s(-1)^m\sinh^2(\gamma_s L)}{L(\gamma_s^2+\eta_m^2)}\left[\frac{\eta_m^2}{\gamma_s^2+\eta_m^2}\left(1+\frac{4n^2}{\gamma_s^2R^2}\right)\right.$$
$$\left.-\frac{4n^2\nu}{\gamma_s^2R^2}\right]J_{2n}(\gamma_s R)\Bigg\}\cos(\eta_m z)\Bigg\}\cos(2n\theta). \tag{35}$$

Finally, equating all the coefficients of Eq. (35) to those of Eq. (4) for all terms of z and θ, we have

$$(2\nu-1)C_0 + \nu A_0 = D_{00}/4, \tag{36}$$

$$-2n(2n-1)(H_{0n}+E_{0n})R^{2n-2} + \sum_{s=1}^{\infty}\frac{G_{sn}}{\Lambda_s}\frac{8n^2\nu\gamma_s\sinh^2(\gamma_s L)}{\gamma_s L}\frac{J_{2n}(\gamma_s R)}{\gamma_s^2R^2} = D_{0n}/2, \tag{37}$$

$$A_{mn}\left[2\nu I_{2n}(\eta_m R) - \frac{1}{\eta_m^2}\left[2\frac{\partial^2 I_{2n}(\eta_m R)}{\partial r^2} + R\frac{\partial^3 I_{2n}(\eta_m R)}{\partial r^3}\right]\right] - \frac{B_{mn}}{\eta_m^2}\frac{\partial^2 I_{2n}(\eta_m R)}{\partial r^2} + \frac{2nE_{mn}}{\eta_m^2}\left[\frac{I_{2n}(\eta_m R)}{R^2}\right.$$
$$\left.-\frac{1}{R}\frac{\partial I_{2n}(\eta_m R)}{\partial r}\right] - \sum_{s=1}^{\infty}\frac{G_{sn}}{\Lambda_s}\frac{4\gamma_s(-1)^m\sinh^2(\gamma_s L)}{L(\gamma_s^2+\eta_m^2)}\left[\frac{\eta_m^2}{\gamma_s^2+\eta_m^2}\left(1+\frac{4n^2}{\gamma_s^2R^2}\right) - \frac{4n^2\nu}{\gamma_s^2R^2}\right]J_{2n}(\gamma_s R)$$
$$= \begin{cases} D_{m0}/2 & \text{for } n=0,\ m>0, \\ D_{mn} & \text{for } n>0,\ m>0. \end{cases} \tag{38}$$

By now, all the boundary conditions have been satisfied, and all unknown coefficients can be uniquely determined. More specifically, the unknown constants A_0 and C_0 can be solved from Eqs. (28) and (36) and A_{mn}, B_{mn}, E_{mn} and G_{sn} can be solved from the coupled system of equations (29), (30), (33) and (38). Finally, H_{0n} and E_{0n} can be solved from Eqs. (32) and (37), and C_{sn} and D_{sn} can then be back-calculated from Eqs. (21) and (22). Therefore, the form of the displacement functions given in Eqs. (11) and (12) is indeed appropriate and complete. Numerical results for our analytical solutions are given and discussed in Section 6.

6. Numerical results and discussion

The analytic results given in the previous section involve the solutions of systems of coupled equations for the coefficients of the infinite series. In actual computation, we have to truncate the infinite series and retain only finite number of terms.

In addition, the roots of $J'_{2n}(x) = 0$ play a very important role in our series solution, and therefore it is necessary to calculate the values of these roots accurately and efficiently. Thus, we discuss briefly here our strategy in obtaining these roots. As discussed by Watson (1944), the smallest root λ_s of $J'_{2n}(x) = 0$ can be bounded by

$$\begin{matrix}\sqrt{\{2n(2n+2)\}} & (\text{for } 1\leqslant n\leqslant 2) \\ \sqrt{\{2n(2n+3)\}} & (\text{for } n>2)\end{matrix} < \lambda_s < \sqrt{\{4n(2n+1)\}}. \tag{39}$$

So the first root can be established within this range by using a standard procedure (e.g., Press et al., 1992). Once this first root is obtained, we can generate the subsequent roots efficiently if the following properties are noted (Wei, 1999): (i) The difference between any two non-zero consecutive roots equals approximately π if x is large; (ii) There must exist a root of $J'_{2n-1}(x) = 0$ between any two consecutive roots of $J'_{2n}(x) = 0$; (iii) Consequently, there must exist a root of $J'_{2n}(x) = 0$ between any two consecutive roots of $J'_{2n-1}(x) = 0$.

Numerical calculations show that the system of equations for solving A_{mn}, B_{mn}, E_{mn} and G_{sn} becomes ill-conditioned for large m and s. More specifically, the coefficients for A_{mn}, B_{mn} and E_{mn} become relatively large compared to those for G_{sn}. Thus, a proper scaling of the coefficient is proposed to alleviate the problem of ill-conditioning. In particular, we divide all coefficients for A_{mn}, B_{mn} and E_{mn} with $I_{2n}(\eta_m R)$ and multiply all coefficients for G_{sn} with λ_s(i.e. A_{mn}, B_{mn} and E_{mn} are scaled by multiplying $I_{2n}(\eta_m R)$, whereas G_{sn} is scaled by dividing λ_s), and after solving A_{mn}, B_{mn}, E_{mn} and G_{sn}, all solutions of A_{mn}, B_{mn} and E_{mn} are divided by $I_{2n}(\eta_m R)$ while the solution for G_{sn} is multiplied by λ_s. We found that more terms in m than in n are needed for acquiring the same degree of convergence for σ_{zz}, while more terms in n than in m are needed for acquiring the same degree of convergence for $\sigma_{\theta\theta}$. In general, 50 terms in n and 25 terms in each of m and s are needed to control the error of tensile stresses σ_{zz} and $\sigma_{\theta\theta}$ to within 1%.

Before we discuss the distribution of the tensile stress within the cylinder, it is instructive to compare the present solution with the approximation by Wijk (1980) for the tensile stress at the center of the cylinder. Table 1 compares the tensile hoop stresses at the center of the cylinder predicted by Wijk (1980) and by the present solution, for cylinders with geometric ratio $L/D = 1$ and ∞, and for Poisson's ratio $v = 0$, 0.1, 0.2, 0.3, 0.4, and 0.5. In addition, instead of idealizing the two applied point loads to two point forces as Wijk (1980) did, we have considered the contact problem between the indentors and the cylinder. Therefore, our solutions for the hoop stress depend on the values of the Young's modulus and the actual magnitude of the point force at failure. We present in Table 1 the results based on different Young's moduli and point forces for the case of $L/D = 1$. It is clear from Table 1 that Wijk's (1980) solution overestimates the values of the tensile stress (about 4% for $L/D = 1$, and about 0.3% for $L/D \to \infty$). Wijk's (1980) approximation is much better for a longer cylinder than for the case of $L/D = 1$. This is expected because the end surface boundary conditions were satisfied only approximately by Wijk's (1980) solution. Note that when v increases, the tensile hoop stress decreases in magnitude, whereas when E increases, the tensile hoop stress increases in magnitude. Although the increase in P results in a decrease in the hoop stress, double the value in the applied force only leads to a difference of 0.1% in the tensile hoop stress. Therefore, the effect of magnitude of the point force is negligible. Although the approximation by Wijk (1980) is considered to be very accurate, we will show next that the maximum tensile stress is not necessarily at the center of the specimen.

Table 1
Comparison of the theoretical predictions of the normalized tensile hoop stress, $\sigma_{\text{center}}/(P/D^2)$, at the center of a solid circular cylinder under the diametral PLST given by Wijk (1980) and by the present study[a]

Poisson's ratio	$L/D = 1.0$				$L/D \to \infty$	
	Wijk (1980)	Present			Wijk (1980)	Present ($E = 70$ GPa $P = 20$ kN)
		$E = 40$ GPa, $P = 10$ kN	$E = 70$ GPa $P = 10$ kN	$E = 70$ GPa $P = 20$ kN		
0.0	0.7678	0.7360	0.7365	0.7358	0.7372	0.7352
0.1	0.7144	0.6865	0.6870	0.6863	0.6877	0.6858
0.2	0.6685	0.6436	0.6441	0.6435	0.6448	0.6430
0.3	0.6284	0.6061	0.6066	0.6060	0.6072	0.6056
0.4	0.5931	0.5730	0.5734	0.5729	0.5740	0.5725
0.5	0.5618	0.5435	0.5439	0.5434	0.5444	0.5431

[a] Note that the results by Wijk (1980) were re-calculated to four significant digits.

Figs. 2 and 3 plot the normalized stresses $\sigma_{\theta\theta}/\sigma_0, \sigma_{zz}/\sigma_0$, and σ_{rr}/σ_0 (where $\sigma_0 = P/D^2$) versus the normalized distance r/R for various sizes of contact zone r_0/R (where r_0 is a nominal radius for the elliptical contact area between the spherical heads of the indentors and the curved surface of the cylinder and is defined as $r_0 = \sqrt{ab}$). The plots are calculated for the standardized size and shape of specimens suggested by Broch and Franklin (1972) and by ISRM (1985). More specifically, we have assumed the following parameters: $D = 50$ mm, $2L = 70$ mm, $R_2 = 5$ mm and $v = 0.25$. By following the usual sign convention of continuum mechanics, tension is plotted as positive. As shown in Figs. 2 and 3, both $\sigma_{\theta\theta}/\sigma_0$ and σ_{zz}/σ_0 are tensile along the line joining the two point loads, and a zone of tensile stress concentration is developed at about $r/R \approx 0.9$, compared to the roughly constant value at the central portion of the line (say for $r/R < 0.6$). Both figures show that the smaller the loading area, the larger the maximum tensile stress in-

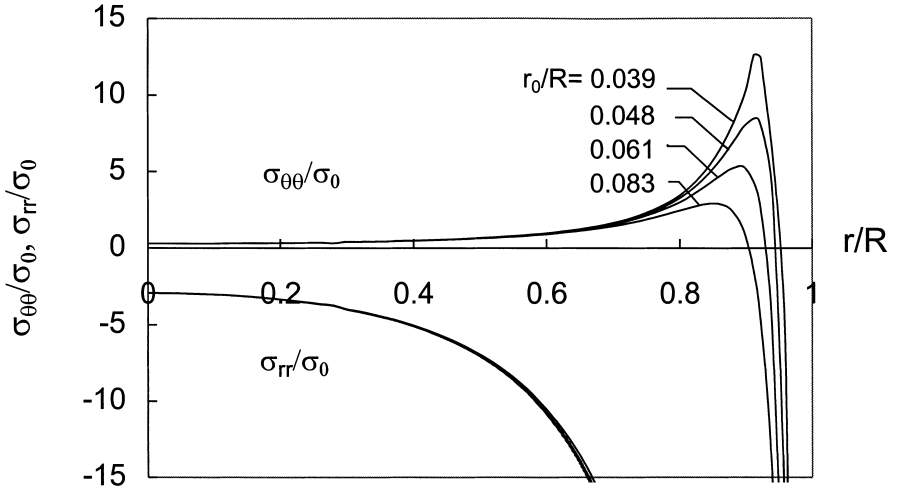

Fig. 2. The normalized stresses $\sigma_{\theta\theta}/\sigma_0$, and σ_{rr}/σ_0 versus r/R along the line joining the two point forces for various values of r_0/R and for $v = 0.25$, $L/D = 1.4$ and $R_2 = 5$ mm.

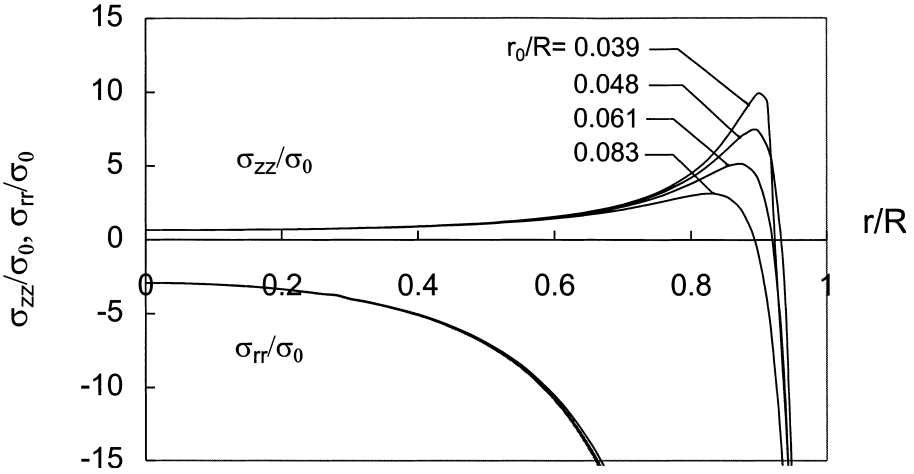

Fig. 3. The normalized stresses σ_{zz}/σ_0, and σ_{rr}/σ_0 versus r/R for various values of r_0/R and for $v = 0.25$, $L/D = 1.4$ and $R_2 = 5$ mm.

duced. It is very interesting to note that both the tensile stress distribution ($\sigma_{\theta\theta}/\sigma_0$) and the compressive stress distribution (σ_{rr}/σ_0) along the line joining the two applied point loads are remarkably similar to those in a sphere under the diametral PLST (Wei and Chau, 1998; Chau and Wei, 1999) and of a cylinder under the axial PLST (Wei et al., 1999). Note that, as suggested by experimental observations, it is commonly believed that specimens fail catastrophically in tensile fracture under diametral PLST. And the results for the axial and hoop stresses given in Figs. 2 and 3 further verify this observation analytically.

Since both the hoop stress $\sigma_{\theta\theta}$ and the axial stress σ_{zz} are tensile, it is necessary to check which one is the maximum tensile stress and thus responsible for the tensile failure of the specimen. Therefore, Fig. 4 compares the normal stresses ($\sigma_{\theta\theta}/\sigma_0, \sigma_{zz}/\sigma_0$ and σ_{rr}/σ_0) in a typical specimen along the normalized distance r/R. The plot is for $r_0/R = 0.039$ and other parameters are the same as those used in Fig. 2. For this case, σ_{zz}/σ_0 is larger than $\sigma_{\theta\theta}/\sigma_0$ in the central part, but $\sigma_{\theta\theta}/\sigma_0$ increases faster than σ_{zz}/σ_0 when the point loads are approached. Consequently, the maximum tensile stress of the specimen is controlled by $\sigma_{\theta\theta}/\sigma_0$, and this maximum tensile stress is usually induced at about $r/R = 0.9$. Therefore, for the following numerical results, only $\sigma_{\theta\theta}/\sigma_0$ is plotted if the standard geometric ratio $2L/D = 1.4$ is used. However, it should be noted that the hoop stress is not always the dominant tensile stress; when Poisson's ratio is relatively large, with $2L/D < 1.4$ and $r_0/R > 0.083$, the maximum tensile stress in a specimen may be controlled by σ_{zz}/σ_0. However, for the specific parameters used in Figs. 5 and 6, the hoop stress is always the dominant tensile stress. Therefore, only the tensile hoop stress (not the axial stress) will be given for Figs. 5 and 6.

The effect of Poisson's ratio on the stress distribution is illustrated in Fig. 5, which plots the normalized stresses $\sigma_{\theta\theta}/\sigma_0$ and σ_{rr}/σ_0 versus the normalized distance r/R for various Poisson's ratio v. The loading area is fixed at $r_0/R = 0.039$, and parameters used are the same as those given in Fig. 2. The smaller the Poisson's ratio, the larger the maximum tensile stress induced. But the tensile stress at the central part along the line of loading and the compressive stress distribution along the same line are insensitive to the change of Poisson's ratio. It is interesting to note that the maximum tensile stress concentrations near the point loads disappear and thus the maximum tensile stress is at the center when the solid becomes incompressible ($v = 0.5$).

The size effect of the spherical head of the indentor (R_2) is demonstrated in Fig. 6, which plots the normalized stresses $\sigma_{\theta\theta}/\sigma_0$ and σ_{rr}/σ_0 versus the normalized distance r/R for various values of R_2 and for $r_0/R = 0.039$. Except for varying R_2, the plots are the same as those given in Fig. 2. As expected, a smaller radius of the spherical head R_2 leads to a higher tensile stress concentration. For example, the maximum

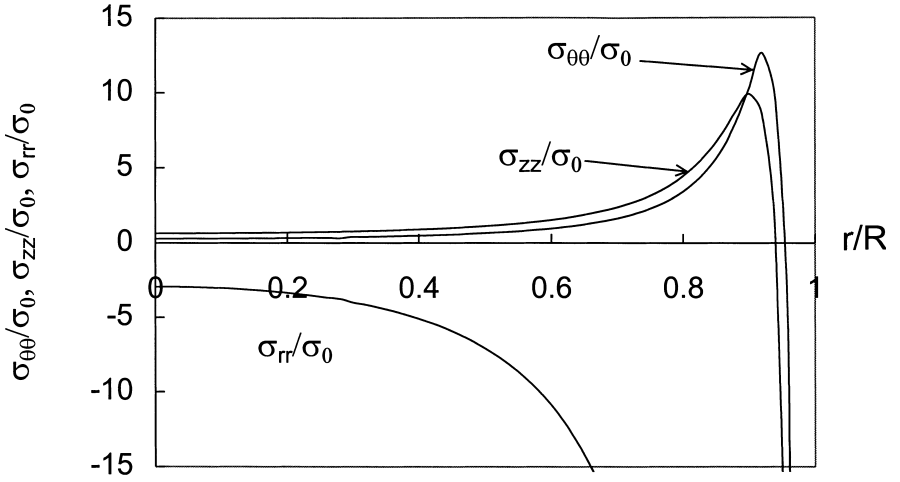

Fig. 4. A typical stress distribution of the normalized stresses $\sigma_{\theta\theta}/\sigma_0, \sigma_{zz}/\sigma$ and σ_{rr}/σ_0 versus r/R for $v = 0.25$ and $r_0/R = 0.039$.

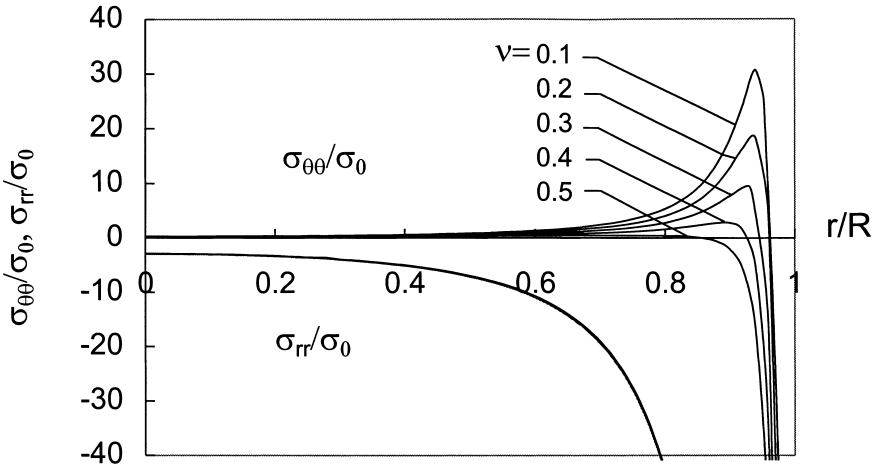

Fig. 5. The normalized stresses $\sigma_{\theta\theta}/\sigma_0$, and σ_{rr}/σ_0 versus r/R for various values of v and $r_0/R = 0.039$.

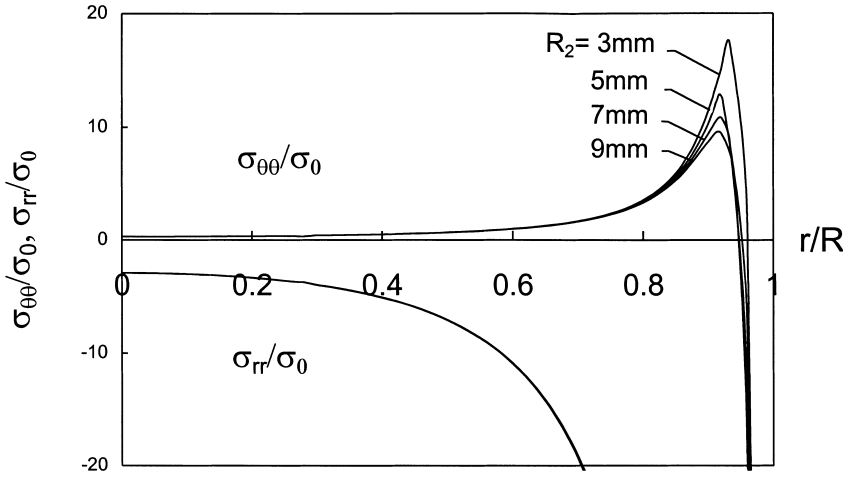

Fig. 6. The normalized stresses $\sigma_{\theta\theta}/\sigma_0$, and σ_{rr}/σ_0 versus r/R for various values of R_2 and $r_0/R = 0.039$.

tensile stress may increase by 35% if $R_2 = 3$ mm is used instead of the standard size of $R_2 = 5$ mm (ISRM, 1985).

Fig. 7 shows the maximum normalized stresses $\sigma_{\theta\theta}/\sigma_0$ and σ_{zz}/σ_0 (which appear at about $r/R = 0.9$) versus half length to diameter ratio L/D for different Poisson's ratio v and for $D = 50$ mm. The solid lines are for the maximum value of $\sigma_{\theta\theta}/\sigma_0$ and the dotted lines are for those of σ_{zz}/σ_0. The maximum value of σ_{zz}/σ_0 decreases drastically with the increase of L/D while the drop of $\sigma_{\theta\theta}/\sigma_0$ with L/D is relatively gentle. Consequently, for $v = 0.25$ the axial stress is the dominant tensile stress for $L/D < 0.4$ and the hoop stress becomes dominant for larger L/D, and for $v = 0.35$ the geometric ratio L/D that separates the dominance between the axial and hoop stresses equals 0.7. Note that v-dependency of the tensile stress is the same as that shown in Fig. 5. Since a larger tensile stress concentration implies a smaller PLSI ($I_s = P_{\max}/D^2$, where $P_{\max}$ is the applied point force at failure), a clear shape effect of PLSI is observed in Fig. 7. This shape dependency has been observed repeatedly on natural rocks (Broch and Franklin, 1972; Greminger, 1982).

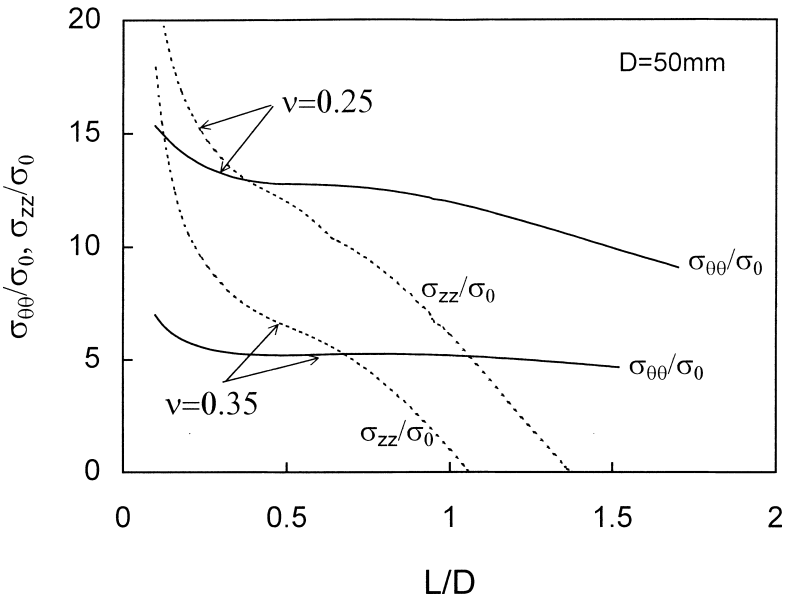

Fig. 7. The maximum normalized tensile stresses $\sigma_{\theta\theta}/\sigma_0$, and σ_{zz}/σ_0 versus L/D for various values of v and for $D = 50$ mm and $r_0/R = 0.039$. The dotted and solid lines are for the axial and hoop stresses respectively.

To further illustrate the shape effect on the maximum tensile stress (i.e. the maximum among the axial and hoop stresses), Fig. 8 plots the maximum stress envelope versus L/D for various values of Poisson's ratio. For $v > 0.25$, the maximum tensile stress is insensitive to the shape as long as $L/D > 0.7$, but for $v = 0.08$, the maximum tensile stress continues to decrease even for $L/D > 0.7$. This illustrates that the shape effect is more severe for more compressible solids or rocks (i.e. rocks with small Poisson's ratio).

Fig. 9 shows these tensile stress envelopes versus L/D for different diameters of the specimens. The size effect is apparent and such an effect has been observed repeatedly in experiments (e.g. Broch and Franklin, 1972; Brook, 1980). For specimen size smaller than 50 mm, the shape effect can be neglected if the L/D is larger than 0.4, but, for larger specimen (say $D = 80$ mm) the maximum stress continues to decrease even for $L/D > 0.7$, which is a value recommended by Broch and Franklin (1972) to remove the shape effect. To avoid this shape effect, ISRM (1985) recommended a value of $L/D > 0.5$ while Broch and Franklin (1972) suggested a value of $L/D > 0.7$. Our analytic solutions show, however, that if Poisson's ratio is small (say $v < 0.1$) and the size of the cylinder is large (say $D = 80$ mm), the shape effect cannot be ignored even for $L/D > 0.7$. Therefore, either large specimen size should be avoided for the diametral PLST or a correction factor for size effect must be applied even for $L/D > 0.7$. It is important that this theoretical prediction should further be verified by experiments because it differs from the recommendation by ISRM (1985) (i.e. $L/D > 0.7$ was recommended to remove shape effect regardless of the size).

7. Experimental validation

A series of the diametral PLST were carried out on cylinders of a rock-like plaster material. A total of over 40 cylinders were cast using a plastic hollow mould of various size ($D = 35$, 40, 50, and 56 mm) and shape factors ($L/D = 0.4$, 0.5, 0.63, 0.76, 0.86 and 1.0). These specimens were made of a water–plaster mixture with water/plaster mass ratio of 3/10; other mechanical properties for the material are $v = 0.25$,

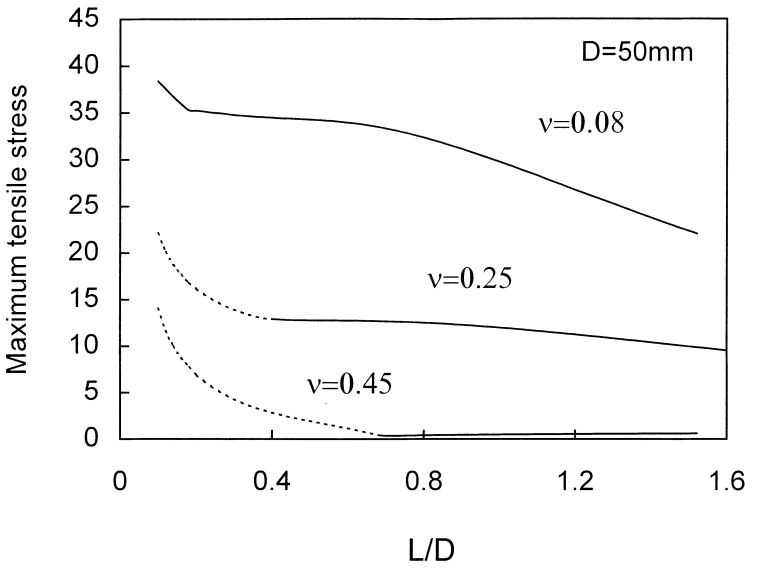

Fig. 8. The maximum tensile stress envelopes versus L/D for various values of v and for $D = 50$ mm. The dotted and solid lines are for axial and hoop stresses respectively.

$E = 17.5$ GPa, the uniaxial compressive strength (UCS) $= 57.54$ MPa, and density $= 1.75$–1.78 g/cm^3. When the plaster mixture was poured into the mould layer by layer, it was tapped by using a small wooden hammer to minimize the content of air and to achieve a homogeneous solid with reproducible properties. The tests were carried out after all the samples were cured for 60 days and had attained a constant weight. For more discussion on the requirements of judging a rock-like material using the Buckingham pi-theorem, we refer to Wong and Chau (1998).

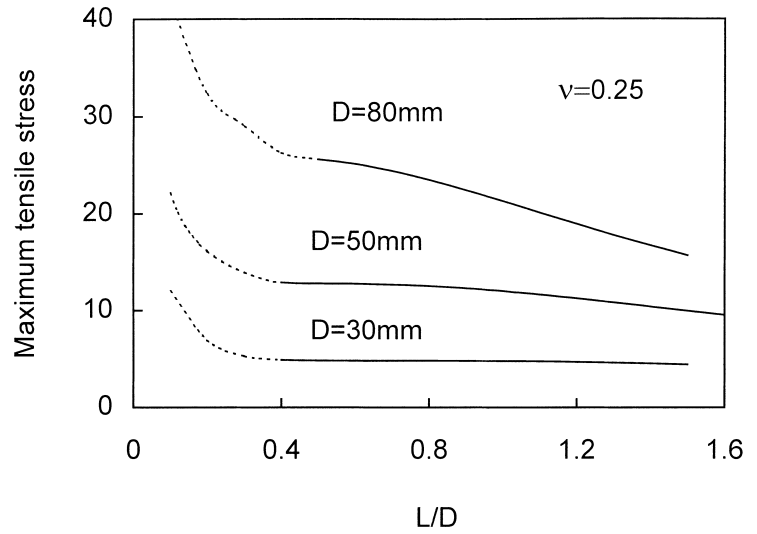

Fig. 9. The maximum tensile stress envelopes versus L/D for various values of D and for $v = 0.25$. The dotted and solid lines are for axial and hoop stresses respectively.

To determine the maximum allowable local tensile stress of the plaster material under the diametral PLST, the theoretical stress profiles of three specimens with $D = 56$ mm and $L/D = 1.4$ were calculated using our analytic solution. The magnitudes of the point forces at the failure of each specimen, together with other elastic properties of the material, were substituted into our solution. Fig. 10 shows the predicted stress profiles for $\sigma_{\theta\theta}, \sigma_{zz}$ and σ_{rr} versus the normalized distance r/R. Stress profiles for these three specimens basically overlap and cannot be distinguished easily on the figure. The calculated maximum tensile stresses for these specimens are 26.1, 25.9 and 26.3 MPa with an average of 26.1 MPa, corresponding to failure loads of 5.54, 5.37 and 5.73 kN. In order to predict the failure load for samples of other size and shape, we assume that if the maximum tensile stress in the solid reaches 26.1 MPa (which will be called the local tensile strength hereafter), the specimen fails. From a microscopic point of view, this assumption implies that a critical local tensile stress of 26.1 MPa is needed to initiate unstable crack growth within the sample. It should be noted that this critical tensile stress is different from the uniaxial tensile strength of solid for which there is no orthogonal compressive stress associated with. To see whether this assumption of "local tensile strength" is valid or not, the size and shape effects predicted by using this assumption are considered next.

By using this local tensile strength, the maximum point force, and hence the PLSI, can be predicted for specimens of any shape and size. Fig. 11 plots the predicted PLSI (or I_s) versus L/D together with our experimental results for specimens of $D = 56$ mm. Basically, theoretical prediction agrees well with experiments. Our theoretical calculations show a very strong shape effect for $L/D < 0.3$ for $D = 56$ mm. As remarked earlier, this shape effect has been observed in other experimental studies (e.g. Broch and Franklin, 1972; Greminger, 1982). Note that for $L/D < 0.2$, it is very difficult to prepare a homogeneous specimen because of the thin thickness. Thus, the predicted sharp drop in I_s may not be verified easily by experiments.

The predicted size effect together with our experimental data on the PLSI is shown in Fig. 12. Specimens of diameter of 35, 40, 50, and 56 mm were tested. The trends of the predicted and observed size effects agree very well. The experimental results appear to be systematically smaller than the theoretical predictions. The reason for this is not known, but it may be related to the additional size effect due to the microstructures of the solid as compared to the size effect considered here, induced primarily by the size of the contact zone between the specimen and the indentor.

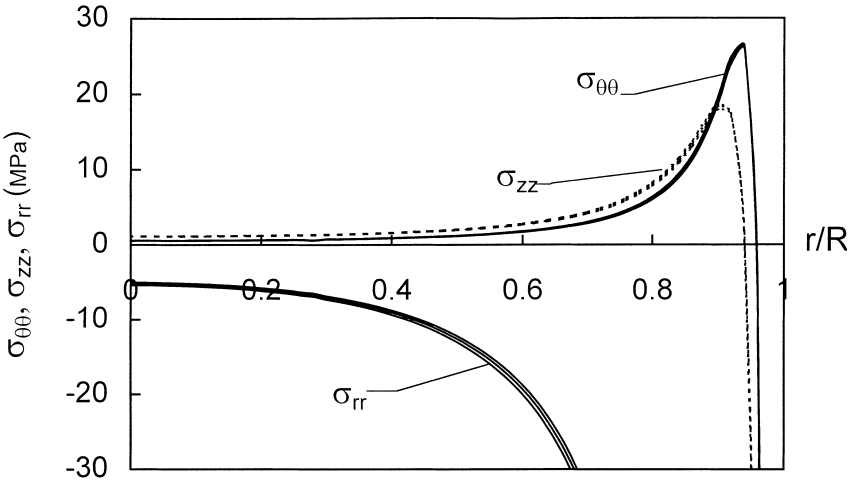

Fig. 10. The theoretical stress distributions for $\sigma_{\theta\theta}, \sigma_{rr}$ and $\sigma_{\theta\theta}$ versus r/R for three plaster specimens of size $D = 56$ mm ($\nu = 0.25$ and $E = 17.5$ GPa).

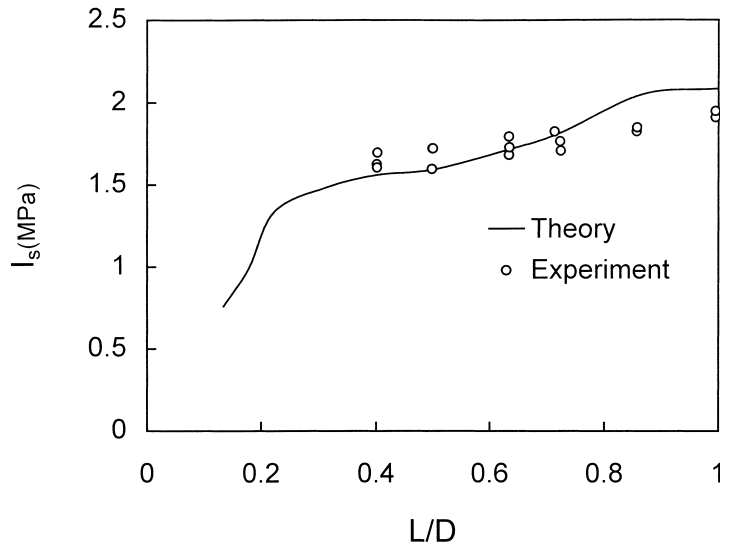

Fig. 11. The theoretical and experimental point load strength index ($I_s = P/D^2$) versus the geometric ratio L/D for the rock-like plaster material and for $D = 56$ mm.

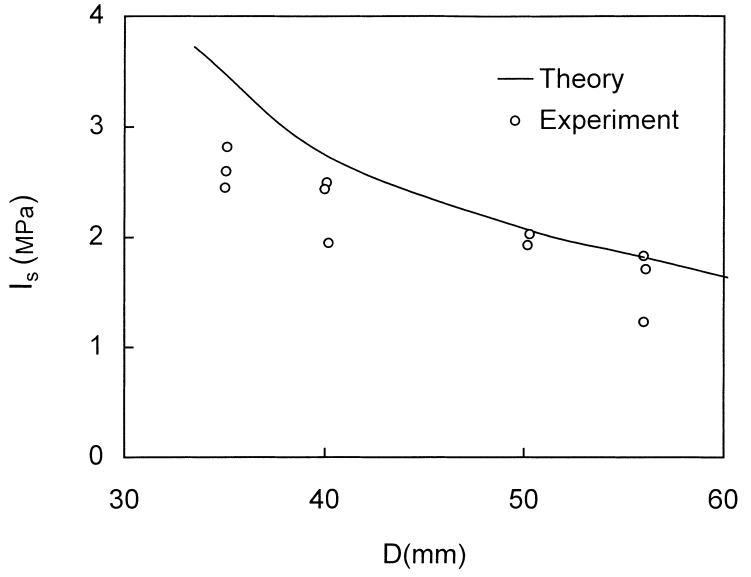

Fig. 12. The theoretical and experimental point load strength index ($I_s = P/D^2$) versus the diameter D for the rock-like plaster material for $L/D = 0.7$.

Fig. 4(a) of ISRM (1985) shows the typical modes of failure of specimens under the diametral PLST observed in experiments. In particular, specimens are normally broken into two or three pieces. The relation between these modes of failure in the PLST and the shape of the specimens has not been studied

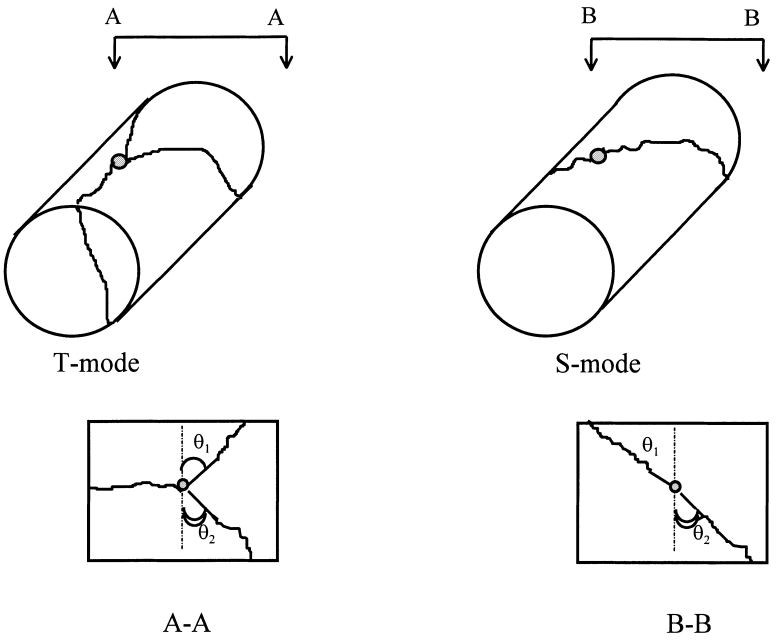

Fig. 13. A sketch of the two failure modes (T-mode and S-mode) of cylinders under the diametral point load strength test (θ_1 and θ_2 are defined as the two minimum angles between the cracks and the transverse line joining the two applied point loads).

before, and the main reason is probably due to the lack of information on the tensile stress field inside the specimens.

Fig. 13 sketches two typical modes of failure observed in our experiments (we call them T-mode and S-mode for indicating Tri-fracture and Single-fracture in the failure mechanism), while Table 2 tabulates the failure mode and pattern for 9 particular samples that we have tested. One should not confuse the S-mode with the shear type failure. In fact, all these failures observed in the diametral test are tensile in nature because both the axial and hoop stresses are, as illustrated earlier, tensile in nature. It is observed that for cylinders with $L/D = 0.4$, T-mode is more likely to occur, while for cylinders with $L/D \geqslant 0.5$, S-mode appears to be dominant. Note that out of the 36 samples with $L/D \geqslant 0.5$ that we have tested, only three

Table 2
Summary of some of the observed failure patterns[a]

Sample no.	L/D	I_s (MPa)	Failure mode	θ_1 (°)	θ_2 (°)
1	0.40	1.69	T	8	50
2	0.40	1.64	T	25	50
3	0.40	1.68	T	50	30
4	0.40	1.54	S	18	18
5	0.50	1.73	S	45	45
6	0.63	1.74	S	60	80
7	0.70	1.88	S	60	60
8	0.86	1.85	S	35	45
9	1.00	1.86	S	35	60

[a] The T-mode and S-mode are depicted in Fig. 13 and θ_1 and θ_2 are defined as the two minimum angles between the cracks and the transverse line joining the two applied point loads.

samples failed in the T-mode. This observation can be explained by checking the numerical results showed in Fig. 8. In particular, for $L/D = 0.4$ and $v = 0.25$, Fig. 8 shows that the magnitudes of $\sigma_{\theta\theta}$ and σ_{zz} are comparable. That is, tensile failure is likely to occur along both axial and transverse directions; thus, multi-fracture shown in the T-mode of Fig. 13 is more likely to occur than the S-mode. However, for longer cylinders (say $L/D \geqslant 0.5$) the tensile stress envelope shown in Fig. 8 suggests that the maximum tensile stress is always dominated by $\sigma_{\theta\theta}$; thus, we speculate that a single fracture may be more likely to occur. However, more elaborated analysis and experiments are still required to make our conclusion more definite.

8. Conclusion

This paper presents a new analytic solution for the stresses inside an isotropic solid circular cylinder of finite length subjected to diametral PLST. The method of solution uses the displacement function approach together with double Fourier expansion for the contact stress, which is obtained by considering the Hertz contact problem between the indentors and the curved surface of the cylinder. Appropriate forms for the displacement functions are proposed so that all boundary conditions and all governing equations can be satisfied. Numerical results show that, similar to the results for a sphere under the diametral PLST or a cylinder under the axial PLST, tensile stress concentrations are developed near the point loads. The maximum tensile stress decreases with the increase of Poisson's ratio, the contact area, the radius of spherical heads of the indentors, but increases with the increase of diameter D. The hoop stress is the dominant tensile stress for long cylinders (say $L/D > 0.7$), but the axial stress may become dominant if L/D is small (say <0.4). The proximity of the values of normal stresses ($\sigma_{\theta\theta}$ and σ_{zz}) also provide a plausible explanation why specimens break into three pieces for $D/L = 0.4$, but into two pieces when $D/L > 0.5$. Both size and shape effects of specimens on the PLSI, which is defined as P/D^2, are predicted by our solution, and these predictions agree well with our experiments. For specimens with large diameter size (say $D = 80$ mm), the shape effect is not negligible even for $L/D > 0.7$. Therefore, specimens with large diameter are not recommended for the diametral PLST. In addition to the practical application to the diametral PLST, the present study should also provide a general solution technique for the stress analysis of cylinders under arbitrary normal stress on the curved surface and zero traction on the two end surfaces.

Acknowledgements

This research was supported by the Research Grants Council (RGC) of the Hong Kong SAR Government under the competitive earmarked research grant (CERG) No. PolyU 70/96E. This work constitutes part of the Ph.D thesis of XXW under the supervision of KTC.

Appendix A. Stresses in terms of the displacement functions

$$\sigma_{rr} = -2vG\nabla^2 \frac{\partial \Phi}{\partial z} + 2G\left[\frac{\partial^3 \Phi}{\partial z \partial r^2} + \frac{\partial}{\partial r}\left(\frac{1}{r}\frac{\partial \Psi}{\partial \theta}\right)\right], \tag{A.1}$$

$$\sigma_{\theta\theta} = -2vG\nabla^2 \frac{\partial \Phi}{\partial z} + 2G\left[\frac{1}{r}\frac{\partial^2 \Phi}{\partial z \partial r} + \frac{1}{r^2}\frac{\partial^3 \Phi}{\partial \theta^2 \partial z} - \frac{\partial}{\partial r}\left(\frac{1}{r}\frac{\partial \Psi}{\partial \theta}\right)\right], \tag{A.2}$$

$$\sigma_{zz} = -2G\left[(2-\nu)\frac{\partial}{\partial z}\nabla^2 - \frac{\partial^3}{\partial z^3}\right]\Phi, \tag{A.3}$$

$$\sigma_{rz} = 2G\left[-(1-\nu)\frac{\partial}{\partial r}\nabla_1 + \nu\frac{\partial^3}{\partial r\,\partial z^2}\right]\Phi + \frac{G}{r}\frac{\partial^2\Psi}{\partial\theta\,\partial z} \tag{A.4}$$

$$\sigma_{Z\theta} = 2G\left[-(1-\nu)\frac{1}{r}\frac{\partial}{\partial\theta}\nabla_1 + \nu\frac{1}{r}\frac{\partial^3}{\partial\theta\,\partial z^2}\right]\Phi - G\frac{\partial^2\Psi}{\partial r\,\partial z}, \tag{A.5}$$

$$\sigma_{r\theta} = 2G\left[\frac{\partial}{\partial r}\left(\frac{1}{r}\frac{\partial^2\Phi}{\partial\theta\,\partial z}\right) + \frac{1}{2}\left(\frac{1}{r}\frac{\partial\Psi}{\partial r} + \frac{1}{r^2}\frac{\partial^2\Psi}{\partial\theta^2} - \frac{\partial^2\Psi}{\partial r^2}\right)\right]. \tag{A.6}$$

Appendix B. Fourier–Bessel expansion for $I_{2n}(\eta_m r)$ and $\eta_m r I_{2n-1}(\eta_m r)$

By applying Fourier–Bessel expansion (Watson, 1944), $I_{2n}(\eta_m r)$ and $\eta_m r I_{2n-1}(\eta_m r)$ involved in Eq. (23) can be expressed in terms of $J_{2n}(\gamma_s r)$ as

$$I_{2n}(\eta_m r) = \sum_{s=1}^{\infty} T_{ms} J_{2n}(\gamma_s r), \tag{B.1}$$

$$\eta_m r I_{2n-1}(\eta_m r) = \sum_{s=1}^{\infty} U_{ms} J_{2n}(\gamma_s r), \tag{B.2}$$

where

$$T_{ms} = \frac{2\lambda_s^2}{R^2(\lambda_s^2 - 4n^2)J_{2n}^2(\lambda_s)}\int_0^R r I_{2n}(\eta_m r) J_{2n}(\gamma_s r)\,\mathrm{d}r, \tag{B.3}$$

$$U_{ms} = \frac{2\lambda_s^2}{R^2(\lambda_s^2 - 4n^2)J_{2n}^2(\lambda_s)}\int_0^R \eta_m r^2 I_{2n-1}(\eta_m r) J_{2n}(\gamma_s r)\,\mathrm{d}r. \tag{B.4}$$

Note again that $\gamma_s = \lambda_s/R$ and λ_s is the root of $J'_{2n}(\lambda_s) = 0$. To integrate (B.3) exactly, we first note the following formula (5.54.1 of Gradshteyn and Ryzhik, 1980):

$$\int_0^R r J_{2n}(\eta_m r) J_{2n}(\gamma_s r)\,\mathrm{d}r = \frac{\eta_m R J_{2n+1}(\eta_m R) J_{2n}(\lambda_s) - \lambda_s J_{2n}(\eta_m R) J_{2n+1}(\lambda_s)}{\eta_m^2 - \gamma_s^2} \tag{B.5}$$

and the following identities

$$I_{2n}(\eta_m r) = (-1)^n J_{2n}(\mathrm{i}\eta_m r) \tag{B.6}$$

$$I_{2n+1}(\eta_m r) = -\mathrm{i}(-1)^n J_{2n+1}(\mathrm{i}\eta_m r) \tag{B.7}$$

Substitution of Eqs. (B.6) and (B.7) into Eq. (B.5) and then into Eq. (B.3) yields Eq. (26) given in the text. To see the validity of Eq. (27), we first consider the following derivatives:

$$\frac{\mathrm{d}}{\mathrm{d}r}[r^2 I_{2n}(\eta_m r)J_{2n}(\gamma_s r)] = 2(1-2n)rI_{2n}(\eta_m r)J_{2n}(\gamma_s r) + r^2[\eta_m I_{2n-1}(\eta_m r)J_{2n}(\gamma_s r) + \gamma_s I_{2n}(\eta_m r)J_{2n-1}(\gamma_s r)] \tag{B.8}$$

and

$$\frac{\mathrm{d}}{\mathrm{d}r}[r^2 I_{2n-1}(\eta_m r)J_{2n-1}(\gamma_s r)] = 4nrI_{2n-1}(\eta_m r)J_{2n-1}(\gamma_s r) + r^2[\eta_m I_{2n}(\eta_m r)J_{2n-1}(\gamma_s r) - \gamma_s I_{2n-1}(\eta_m r)J_{2n}(\gamma_s r)]. \tag{B.9}$$

We then consider the integration of an equation resulting from the subtraction of Eq. (B.9) $\times \gamma_s$ from Eq. (B.8) $\times \eta_m$, and by virtue of Eq. (26) the expression given in Eq. (27) can be derived.

References

Bieniawski, Z.T., 1975. The point test in geotechnical practice. Engng. Geol. 9, 1–11.

Broch, E., Franklin, J.A., 1972. The point load strength test. Int. J. Rock Mech. Min. Sci. 9, 669–697.

Brook, N., 1980. Size correction for point load testing. Int. J. Rock Mech. Min. Sci. Geomech. Abstr. 17, 231–235.

Chau, K.T., 1997. Young's modulus interpreted from compression tests with end friction. J. Engng. Mech. ASCE 123 (1), 1–7.

Chau, K.T., 1998. Analytic solutions for diametral point load strength tests. J. Eng. Mech. ASCE 124 (8), 875–883.

Chau, K.T., Wei, X.X., 1999. Spherically isotropic, elastic spheres subject to diametral point load strength test. Int. J. Solids and Struct. 36 (29), 4473–4496.

Chau, K.T., Wong, R.H.C., 1996. Uniaxial compressive strength and point load strength of rocks. Int. J. Rock Mech. Min. Sci. Geomech. Abstr. 33 (2), 183–188.

Chree, C., 1889. The equations of an isotropic elastic solid in polar and cylindrical co-ordinates, their solution and application. Camb. Phil. Trans. 14, 250.

Dougall, J., 1914. An analytic theory of the equilibrium of an isotropic elastic rod of circular section. Trans. Roy. Soc. Edin. 59 (4), 895–978.

Filon, L.N.G., 1902. On the elastic equilibrium of circular cylinders under certain practical systems of load. Phil. Trans. Roy. Soc. 198, 147–223.

Gradshteyn, I.S., Ryzhik, I.M. 1980. Table of integrals, series, and products. Academic Press, New York, NY.

Greminger, M., 1982. Experimental studies of the influence of rock anisotropy on size and shape effects in point-load testing. Int. J. Rock Mech. Min. Sci. Geomech. Abstr. 19, 241–246.

Hassani, F.P., Scoble, M.J., Whittaker, B.N., 1980. Application of the point load index test to strength determination of rock and proposals for a new size-correction chart. The state of the art in rock mechanics. In: Proceedings of the 21st US Symposium on Rock Mechanics. Rolla, Missouri, pp. 543–553.

Hiramatsu, Y., Oka, Y., 1966. Determination of the tensile strength of rock by a compression test of an irregular test piece. Int. J. Rock Mech. Min. Sci. 3, 89–99.

ISRM, 1985. Suggested method for determining point load strength. Int. J. Rock Mech. Min. Sci. Geomech. Abstr. 22, 53–60.

Ogaki, Y., Nakajima, N., 1983. Stress analysis of a circular cylinder of finite length subjected to loads symmetrical to middle plane and to axis of revolution. Sci. Engng. Rev. Doshisha Univ. 23 (4), 195–205.

Peng, S.S., 1976. Stress analysis of cylindrical rock discs subjected to axial double point load. Int. J. Rock Mech. Min. Sci. Geomech. Abstr. 13, 97–101.

Pochhammer, L., 1876. Beitrag zur theorie der biegung des Kreiscylinders. Crelle's J. 81, 33.

Press, W.H., Flannery, B.P., Teukolsky, S.A., Vetterling, W.T., 1992. Numerical recipes: the art of scientific computing, second ed. Cambridge University Press, New York.

Saito, H., 1952. The axially symmetrical deformation of a short cylinder. Trans. JSME 18 (68), 21–28.

Saito, H., 1954. The axially symmetrical deformation of a short cylinder. Trans. JSME 20 (91), 185–190 (in Japanese with English abstract).

Sternberg, E., Rosenthal, F., 1952. The elastic sphere under concentrated loads. J. Appl. Mech. ASME 19, 413–421.

Watson, G.N., 1944. A Treatise on the Theory of Bessel Functions, second ed. Cambridge University Press, Cambridge.

Wei, X.X., 1999. Theoretical stress analyses for rock spheres and cylinders under the point load strength test. Ph.D Dissertation, Hong Kong Polytechnic University.

Wei, X.X., Chau, K.T., 1998. Spherically isotropic spheres subject to diametral point load test: analytic solutions. Int. J. Rock Mech. Min. Sci. 35, 4–5.

Wei, X.X., Chau, K.T., Wong, R.H.C., 1999. Analytic solution for axial point load strength test on solid circular cylinders. J. Eng. Mech. ASCE 125 (12), 1349–1357.

Wijk, G., 1978. Some new theoretical aspects of indirect measurements of the tensile strength of rocks. Int. J. Rock Mech. Min. Sci. Geomech. Abstr. 15, 149–160.

Wijk, G., 1980. The point load test for the tensile strength of rock. Geotech. Test. J. 3 (2), 49–54.

Wong, R.H.C., Chau, K.T., 1998. Patterns of coalescence in a rock-like material containing two parallel inclined frictional cracks under uniaxial compression. Int. J. Rock Mech. Min. Sci. 35 (2), 147–164.